Thermoelectric Magnetohydrodynamic Model for Laser-Based Metal Additive Manufacturing

Lu Wang and Wentao Yan*

Department of Mechanical Engineering, National University of Singapore, 117575, Singapore

(Received 1 January 2021; revised 15 April 2021; accepted 4 June 2021; published 21 June 2021)

Magnetic fields are recently being applied to metal additive manufacturing to control the molten pool dynamics and dendritic morphology. To study the molten pool dynamics under an external magnetic field, a thermoelectric magnetohydrodynamic (TEMHD) model is developed by incorporating the electrodynamic model with the Seebeck effect into the multiphysics thermal-fluid flow model. The Seebeck effect in the molten pool is analyzed with the simulation of stationary laser melting on a bare plate. Furthermore, different external magnetic fields are assigned in the TEMHD simulations with the stationary laser melting and the results show that the Lorentz force can damp the keyhole fluctuations. Finally, the laser scanning simulations on a bare plate under external magnetic fields indicate that the Lorentz force can smooth the fluid flow fields in the molten pool and increase the ratio of equiaxed grains in the solidification front.

DOI: 10.1103/PhysRevApplied.15.064051

I. INTRODUCTION

Magnetohydrodynamics (MHD) has been investigated extensively in traditional metal manufacturing processes [1–6]. With the development of metal additive manufacturing, scientists also try to implement magnetic fields into selective laser melting (SLM) [7,8], liquid metal jet printing [9], and drop-on-demand printing [10] to tailor the dendritic morphology and improve the mechanical properties of the as-built part. In MHD, a rotating magnetic field [4,5] can stir the liquid metal to produce a fine-grained as-built part with little or no porosity. Under a static magnetic field, the magnetic damping effect can convert kinetic energy into heat via Joule dissipation to suppress turbulence in the casting molds [6]. In addition to the magnetic stirring and damping effect, the Lorentz force due to the Seebeck effect and external magnetic field can also drive liquid flow in the metal solidification process [11–14]. The MHD with the Seebeck effect is also known as thermoelectric magnetohydrodynamics (TEMHD) [13–15].

As the physical phenomena in TEMHD are diverse, many experiments and numerical studies were conducted to explore the comprehensive electromagnetic effect on metal solidification. On the experimental aspect, the results showed that the grain structure can be influenced by different magnetic fields, such as refined grains with the increase of magnetic intensity [7,12], macrosegregations [16,17], and tilted solidification fronts [14,18]. However, it is difficult to observe the liquid motion and grain growth process in metal additive manufacturing owing to the small-scale molten pool and rapid solidification process. In addition, the electric current, magnetic field, and Lorentz force can hardly be detected, which makes it difficult to analyze the distribution and amplitude of the Lorentz force. On the numerical aspect, Cai *et al.* [14] combined a cellular automaton (CA) model with a fluid dynamics model to simulate the grain growth in a nearly static fluid domain. Chen *et al.* [19] analyzed the thermoelectric effect in the laser welding process with a TEMHD model. Cao *et al.* [20] developed a phase field (PF)-magnetic field (MF)-lattice Boltzmann method (LBM) to predict the solution distribution and dendritic morphology in two dimensions. Kao *et al.* [8] predicted the microstructure evolution in the steady-state molten pool using a CA-based grain growth model.

These previous models either predigested the hydrodynamic process or simplified the electrodynamic process. Thus, these models could not fully reflect the main compositions of electric currents, magnetic field, and Lorentz force in the molten pool, and how the Lorentz force influences the molten pool flow during additive manufacturing. In this paper, a TEMHD model for metal additive manufacturing is built by integrating a multiphysics thermal-fluid flow model with the Marangoni effect, metal evaporation, and ray-tracing heat source model incorporated, and an electrodynamic model with the convection and Seebeck effect as discussed in Sec. II. We then use the model to study the interaction between hydrodynamics and electrodynamics in the molten pool during the metal additive manufacturing process in Sec. III. The stationary laser melting process is simulated to analyze the Lorentz force by the Seebeck effect on the molten pool dynamics;

*Corresponding author. mpeyanw@nus.edu.sg

moreover, the composition and distribution of the electric currents, magnetic fields, Lorentz forces, and molten pool dynamics under different external magnetic fields are simulated; finally, the molten pool dynamics in the laser scanning process are simulated to study the influence of external magnetic field on the SLM process.

II. METHODOLOGY

As shown in Fig. 1, the molten pool dynamics in the SLM process with an external magnetic field involves the fluid dynamics, evaporation, heat transfer, and electrodynamics, etc. To simulate these complex phenomena, an electrodynamic model and our previous multiphysics thermal-fluid flow model [21] are combined to build a comprehensive TEMHD model.

A. Multiphysics thermal-fluid flow model

In the multiphysics thermal-fluid flow model, the liquid phase is assumed to be an incompressible Newtonian fluid with laminar flow. The density of the material (ρ) is constant. The mass continuity, momentum conservation, and energy conservation equations are given as follows:

$$\nabla \cdot (\rho \mathbf{v}) = 0 \tag{1}$$

$$\frac{\partial}{\partial t}(\rho \mathbf{v}) + \nabla \cdot (\rho \mathbf{v} \otimes \mathbf{v}) = -\nabla p + \mu \nabla^2 \mathbf{v} + \mathbf{f_B} - D\mathbf{v} + \mathbf{f_{lz}} \tag{2}$$

$$\frac{\partial}{\partial t}(\rho I) + \nabla \cdot (\rho \mathbf{v} I) = \nabla \cdot (k \nabla T) + Q, \tag{3}$$

where μ and k are the temperature-dependent dynamic viscosity and thermal conductivity of the material, $\mathbf{v}$ is the velocity vector, p is the pressure, T is the temperature,

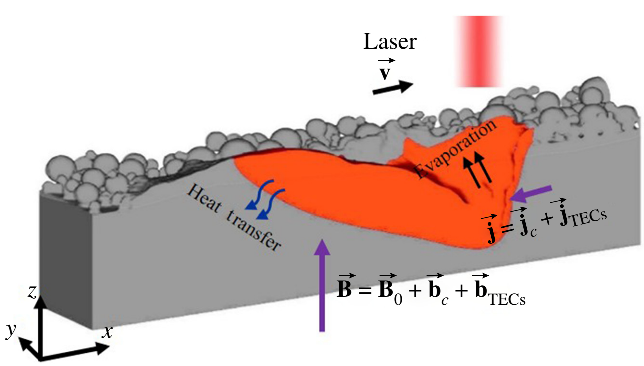

FIG. 1. The multiphysics coupling process in the SLM process under an external magnetic field. The orange domain is the molten pool. Here $\mathbf{B}_0$, $\mathbf{b}_c$, and $\mathbf{b}_{\mathrm{TECs}}$ are the external magnetic field, induced magnetic field by convection and diffusion, and induced magnetic field by the Seebeck effects; $\mathbf{j}_c$ and $\mathbf{j}_{\mathrm{TECs}}$ are the convection-term-induced electric currents and thermoelectric currents.

and Q is the power absorbed by the material. Here $I = C_p T + (1 - F_s) L_m$ is the specific internal energy, where C_p and L_m are the specific heat and latent heat of melting, and F_s is the solid fraction given as follows:

$$\begin{cases} F_s = 1, & \text{if } T \le T_s, \\ F_s = \dfrac{T_l - T}{T_l - T_s}, & \text{if } T_s < T \le T_l, \\ F_s = 0, & \text{if } T_l < T, \end{cases} \tag{4}$$

where T_s and T_l are the solidus and liquidus temperature of the material.

In the momentum conservation equation, the source terms, $\mathbf{f_B}$, $D\mathbf{v}$, and $\mathbf{f}_{lz}$ are the buoyancy force, Darcy drag force, and Lorentz force, respectively. The buoyancy force $\mathbf{f_B}$ is accounted with the Boussinesq approximation

$$\mathbf{f_B} = \rho \mathbf{g} \alpha_v (T - T_l), \tag{5}$$

where $\mathbf{g}$ is the gravitational acceleration vector and α_v is the thermal expansion coefficient of the material. The mushy zone is taken as a porous medium. Based on the Darcy's law, the Darcy drag force ($D\mathbf{v}$) is employed to ensure the rigidity and resistance to flow of the solidified material. The drag coefficient (D) is given as

$$D = C(F_s^2)/((1 - F_s)^3 + B), \tag{6}$$

where C is a constant representing mushy zone morphology, B is the positive zero used to avoid division by zero, so that the Darcy drag force is zero for the molten material and extremely large for the solidified material, and $\mathbf{f_{lz}}$ is the Lorentz force, which is discussed in the electrodynamic model.

To capture the free surface of the molten pool, the volume-of-fluid (VoF) method [22] is adopted

$$\frac{\partial F}{\partial t} + \nabla \cdot (F \mathbf{v}) = 0, \tag{7}$$

where F is the phase fraction.

The recoil pressure and surface tension are incorporated as boundary conditions on the free surface

$$p_s = \sigma(T) K + P_{\mathrm{rec}}(T), \tag{8}$$

where p_s and K are the pressure on the free surface and the curvature of the free surface and $\sigma(T)$ is the temperature-dependent surface tension coefficient

$$\sigma(T) = \sigma_0 - \sigma_s^T (T - T_{\mathrm{ref}}), \tag{9}$$

where σ_0 and σ_s^T are the surface tension coefficient at the reference temperature T_{ref} and temperature sensitivity of $\sigma(T)$. The recoil pressure ($P_{\mathrm{rec}}(T)$), due to the metal evaporation, is derived in our previous work [23]

$$P_{\mathrm{rec}}(T) = \frac{P_e e^{m^2}}{2}(F^- + T^-)(2m^2 + 1), \tag{10}$$

where

$$\begin{cases} m \overset{\mathrm{def}}{=} \sqrt{\dfrac{\gamma}{2}} Ma, \\ F^- = -\sqrt{\pi} m\,[1 - \mathrm{erf}(m)] + e^{-m^2}, \\ T^- = \sqrt{1 + \dfrac{\pi}{64} m^2} - \dfrac{\sqrt{\pi}}{8} m, \end{cases} \tag{11}$$

γ, Ma, P_e, and erf(m) are the heat capacity ratio (for monotonic gases $\gamma = 5/3$), the Mach number of the vapor phase, the saturated vapor pressure, and the Gaussian error function. The saturated pressure is determined by the compositions of the alloy

$$P_e = \sum_i k_i P_i, \tag{12}$$

$$M = \frac{\sum_i M_i k_i P_i}{\sum_i k_i P_i}, \tag{13}$$

where M_i, k_i, and P_i are the molar mass, molar fraction, and saturated pressure of the ith component of the material at the specific temperature. In the current study, AlSi10Mg is used and the compositions are listed in Table I, where the trace elements are ignored.

On the free surface, the heat convection and radiation are incorporated

$$k\nabla T = -h_c(T - T_0) - \epsilon\delta_s(T^4 - T_0^4), \tag{14}$$

where h_c is the heat convection coefficient, δ_s is the Stefan-Boltzmann constant (5.67×10^{-8} W/(m$^2 \cdot$ K^4)), ϵ is the emissivity factor, and T_0 is the ambient temperature. In the multiphysics thermal-fluid flow model, the heat flux within the cross section of the laser is assumed to be Gaussian distributed. The laser is subdivided into a series of rays and incorporated by using the ray-tracing method [24] to track the multireflections of laser. Based on the experiments [25,26], Pei *et al.* [27] built a temperature-dependent laser absorption function ($\alpha(T)$) for aluminum at each reflection

$$\alpha(T) = \begin{cases} 0.7303 \times \left(\dfrac{-1 + 0.0125T}{\lambda_l}\right)^{0.5}, & \text{if } T \le T_l, \\ 0.7303 \times \left(\dfrac{10.7 + 0.0145T}{\lambda_l}\right)^{0.5}, & \text{if } T_l < T \le T_b, \\ 0.7303 \times \left(\dfrac{10.7 + 0.0145T_b}{\lambda_l}\right)^{0.5}, & \text{if } T > T_b, \end{cases} \tag{15}$$

where λ_l is the laser wavelength. As the fraction of aluminum in AlSi10Mg is around 90%, it is reasonable to apply this function to calculate the absorption of AlSi10Mg. The reflected ray with the residual energy will go through subsequent reflections on the molten pool surface until traveling out of the simulation domain or being reflected 20 times (the residual energy is minor enough to be neglected to save the computational cost). The absorbed energy of the laser is the sum of the absorbed energy in all reflections.

It should be clarified that the absorption function is based on the experiment without consideration of the laser incident angle. If the laser energy absorption is calculated by the Fresnel equation with the reflective index of aluminum, the laser absorption of AlSi10Mg is not accurate as of the simulations with other materials [23,28]. The total laser absorption of AlSi10Mg is always lower than 30% and much lower than the experimental results by Trapp *et al.* [29]. It might be the reason that the oxidized elements of AlSi10Mg influence the material reflective index. A more accurate reflective index for AlSi10Mg is required to adopt the Fresnel equation. The multiphysics thermal-fluid flow model has been validated against the experiment in our previous work [21,23,30], which also indicates that the mesh size less or equal to 5 μm can ensure the accuracy of the simulation. Thus, we conduct no more detailed convergence tests in the current work.

TABLE I. Element mass fraction of AlSi10Mg.

	Mass fraction (%)		
Material	Al	Si	Mg
AlSi10Mg	88	10	2

B. Electrodynamic model with the seebeck effect

MHD is concerned with the interaction of electrically conductive, nonmagnetic fluid flow, and magnetic fields. The electrodynamic equations for magnetic and electric current are Ampere's law, Faraday's law, and Ohm's law as follows

$$\nabla \times \mathbf{B} = \mu_0 \mathbf{j}, \tag{16}$$

$$\nabla \times \mathbf{E} = -\frac{\partial \mathbf{B}}{\partial t}, \tag{17}$$

$$\mathbf{j} = \sigma_c(\mathbf{E} + \mathbf{v} \times \mathbf{B}), \tag{18}$$

where $\mathbf{B}$, $\mathbf{j}$, and $\mathbf{E} = -\nabla\phi$ are the magnetic field, electric current, and electric potential gradient, respectively, ϕ is the electric potential, $\mu_0 = 4\pi \times 10^{-7}$ H/m and σ_c are the permeability of vacuum and electric conductivity. Considering the Seebeck effect (thermoelectric effect), Ohm's law has a new term

$$\mathbf{j} = \sigma_c(\mathbf{E} + \mathbf{v} \times \mathbf{B} - \mathrm{Se}\nabla T), \tag{19}$$

where Se is the Seebeck coefficient of the material. In Eq. (19), the term $\mathbf{v} \times \mathbf{B}$ generates the induced electric currents ($\mathbf{j}_c$), whereas $Se\nabla T$ is responsible for the thermoelectric currents (TECs; $\mathbf{j}_{\mathrm{TECs}}$) as shown in Fig. 1(a). Combining Eqs. (16), (17), and (19), the induction equation (magnetic advection-diffusion equation) for TEMHD is given as

$$\frac{\partial \mathbf{B}}{\partial t} = \nabla \times (\mathbf{v} \times \mathbf{B}) - \lambda \nabla \times (\nabla \times \mathbf{B}) - \nabla \times (\mathrm{Se}\nabla T), \tag{20}$$

where $\lambda = 1/(\mu_0 \sigma_c)$ is the magnetic diffusivity. Based on the MHD theory [31], the total magnetic field $\mathbf{B} = \mathbf{B}_0 + \mathbf{b}$ is composed of the external magnetic field ($\mathbf{B}_0$) and induced magnetic field ($\mathbf{b}$), which is due to the electric currents in the media. As shown in Fig. 1(a), the induced magnetic field contains two parts: induced magnetic field ($\mathbf{b}_c$) by the convection term in induction equation, and induced magnetic field ($\mathbf{b}_{\mathrm{TECs}}$) by the Seebeck effects ($-\nabla \times (\mathrm{Se}\nabla T)$).

According to the scalar conservation law, the TEC-induced magnetic field $-\nabla \times (\mathrm{Se}\nabla T)$ is equal to $-\nabla \mathrm{Se} \times \nabla T$. Because the Seebeck coefficient is taken as constant in the same phase (liquid, solid), this source term mainly exists on the interface of different phases with a temperature gradient.

With the magnetic divergence constraint, $\nabla \cdot \mathbf{B} = 0$, the magnetic diffusion term ($-\lambda \nabla \times (\nabla \times \mathbf{B})$) can be simplified as $\lambda \nabla^2 \mathbf{B}$. The diffusion characteristic time of the magnetic field (l_c^2/λ, $\lambda \sim 10^{-1}$ m^2/s, l_c is the characteristic length) is much lower than the diffusion characteristic time in the fluid field ($l_c^2 \rho/\mu$, $\mu/\rho \sim 10^{-6}$ m^2/s). The magnetic Reynolds number is $Re_m = U l_c^2/\lambda \sim 0.01 \ll 1$, where U is the characteristic velocity of the molten pool, which implies that the advection of the magnetic field is negligible.

However, the temperature gradient in the molten pool, which has an effect on the magnetic field, electric currents, and Lorentz force, is not investigated fully. Thus, only the unsteady term of Eq. (20) is ignored to save computational time instead of ignoring induced magnetic field directly. The simplified induction equation for TEMHD is

$$\lambda \nabla^2 \mathbf{B} = (\mathbf{v} \cdot \nabla)\mathbf{B} - (\mathbf{B} \cdot \nabla)\mathbf{v} + \nabla \mathrm{Se} \times \nabla T. \tag{21}$$

Substituting Eq. (19) into the charge conservation equation, $\nabla \cdot \mathbf{j} = 0$, the electric potential equation is given as

$$\nabla^2 \phi = \nabla \cdot (-Se\nabla T + \mathbf{v} \times \mathbf{B}). \tag{22}$$

Therefore, the electric current is obtained by solving the Eq. (22) and (19) sequentially. The magnetic field is calculated with Eq. (21). The Lorentz force, $\mathbf{f}_{lz} = \mathbf{j} \times \mathbf{B}$, can be further applied to the fluid dynamics. It should be specified that this TEMHD model can be readily applied to other laser-based additive manufacturing processes and materials, and we take the SLM process as an example.

The finite volume method (FVM) with the staggered mesh is implemented in the numerical scheme: the value of the magnetic, electric potential, and electric current field are distributed in the center of the control volumes (CVs) and the velocity is on the face of the CVs. The discretized transport equations for multiphysical thermal fluid are implemented in the computational fluid dynamics software FLOW3D. The discretized steady-state induction equation is given as

$$\lambda \nabla^2 \mathbf{B}^{n+1} = (\mathbf{v}^{n+1} \cdot \nabla)\mathbf{B}^n - (\mathbf{B}^n \cdot \nabla)\mathbf{v}^{n+1} + \nabla \mathrm{Se} \times \nabla T^{n+1}, \tag{23}$$

where the variables with the superscript n and $n+1$ are the values at the current time step and next time step, which are also applied to other variables in the paper. The ambient gas is assumed to be insulated. Thus, the numerical induction equation in the gas domain is simplified as

$$\nabla^2 \mathbf{B}^{n+1} = 0. \tag{24}$$

In the alloy domain, the electric potential equation is discretized as

$$\nabla^2 \phi^{n+1} = \nabla \cdot (-\mathrm{Se}\nabla T^{n+1} + \mathbf{v}^{n+1} \times \mathbf{B}^{n+1}). \tag{25}$$

As there is no Seebeck effect or convection in the gas domain, the discretized electric potential equation is given as

$$\nabla^2 \phi^{n+1} = 0. \tag{26}$$

Thus, the calculation of the electric currents and Lorentz force distribution in the domain at next time step are given as

$$\mathbf{j}^{n+1} = \sigma_c(-\nabla \phi^{n+1} + \mathbf{v}^{n+1} \times \mathbf{B}^{n+1} - \mathrm{Se}\nabla T^{n+1}), \tag{27}$$

$$\mathbf{f}_{lz}^{n+1} = \mathbf{j}^{n+1} \times \mathbf{B}^{n+1}. \tag{28}$$

The calculation scheme of the TEMHD model is as follows.

Step 1. Solve the multiphysics thermal-fluid flow Eqs. (1), (2), (3), and (7) to update $\mathbf{v}^{n+1}$, p^{n+1}, T^{n+1}, and F^{n+1}.

Step 2. Move the heat source to the new position and calculate the energy absorption on the free surface with the ray-tracing method.

Step 3. Solve the induction Eqs. (23) and (24), electric potential Eqs. (25) and (26), electric current Eq. (27), and Lorentz force Eq. (28) to update $\mathbf{B}^{n+1}$, ϕ^{n+1}, $\mathbf{j}^{n+1}$, and $\mathbf{f}_{lz}^{n+1}$ with $\mathbf{v}^{n+1}$, T^{n+1}, and F^{n+1}. Repeat Steps 1–3 until the simulation is finished.

III. APPLICATION TO SELECTIVE LASER MELTING

To analyze the molten pool dynamics under magnetic fields, the stationary laser melting and laser scanning processes are simulated. The thermophysical and temperature-dependent thermophysical properties of AlSi10Mg are listed in Tables V and VI, respectively. The ambient pressure and temperature are 1 atm and 300 K. The external magnetic field ($\mathbf{B}_0$) is static due to permanent magnets at 0.4 T based on the previous experiments [7,11]. The laser power and diameter are 300 W and 80 μm, respectively. The mesh size for the stationary laser melting and laser scanning simulations are 2.5 μm and 4 μm, respectively, to ensure accuracy and efficiency. All the simulations are conducted on a workstation with an I9-10900KF CPU. The numerical convergence analysis of the numerical scheme is given in Appendix B.

In Table II, the components of the magnetic fields in the simulations are listed, where the simulation cases with Roman and Arabic numbers represent the stationary laser melting and laser scanning simulation cases, respectively. b series simulation cases are the control groups for the stationary laser melting simulations without incorporating induction equation same as case 2 and 3. In other words, these simulation cases do not include the induced magnetic fields, while including the electric currents only by Eq. (19).

TABLE II. The components of the magnetic fields in the simulations.

Simulation cases	External magnetic field	Induced magnetic field
i-a	0.0 T	Yes
i-b	0.0 T	No
ii-a	0.4 T y direction	Yes
ii-b	0.4 T y direction	No
iii-a	0.4 T z direction	Yes
iii-b	0.4 T z direction	No
1	0.0 T	Yes
2	0.4 T y direction	No
3	0.4 T z direction	No

A. Seebeck effect in the stationary laser melting without external magnetic fields

Without an external magnetic field, the Seebeck effect generates the electric current ($\mathbf{j}$) and induced magnetic field ($\mathbf{b}$), and further transfers the electric energy into the mechanical energy of liquid metal through the work by the Lorentz force. This effect is not accounted for by the previous metal additive manufacturing fluid flow simulations. To analyze the Seebeck effect in metal additive manufacturing, the stationary laser melting simulations i-a and i-b are conducted.

In Fig. 2, the temperature, temperature gradient, and electric current distribution in the middle cross section of the molten pool are given, where Figs. 2(d)–2(f) are the results of the control group (case i-b). The simulation results show that the shapes of the keyhole and molten pool with and without the Seebeck effect are similar. The depths of the keyholes below the plate in cases i-a and i-b at $t = 120$ μs are 155 μm and 142 μm, respectively, and the relative difference between them is 8.4%. For both simulation results, the temperature, temperature gradient, and electric current distribution on the upper and bottom surface of the molten pool are higher than the middle and internal parts of the molten pool as shown in Fig. 2. Such temperature and temperature gradient distributions are caused by the laser energy concentration in the upper and bottom of the keyhole due to the multireflections. The temperature gradients in the molten pools of both simulations range between 1×10^7 K/m and 1×10^8 K/m matching with the previous studies [32,33], and are much higher than that in casting ($1 \times 10^3 - 1 \times 10^4$ K) [34]. This means that the Seebeck effect is much stronger in the laser melting process. The magnitudes of the electric currents in Fig. 2(c) and 2(f) are both $\sim 1 \times 10^8$ A/m^2. As there is no induced magnetic field in Fig. 2(f), the electric current is the TECs ($\mathbf{j}_{\mathrm{TECs}}$). It also suggests that the main electric current of the Seebeck effect in Fig. 2(c) is the TECs, and the induced electric current by the convection ($\mathbf{v} \times \mathbf{B}$) in Eq. (19) can be ignored in the Seebeck effect. Moreover, the magnitude of TECs can be estimated with Ohm's law [19,35],

$$\|\mathbf{j}_{\mathrm{TECs}}\| \sim \sigma_c(\mathrm{Se}_l - \mathrm{Se}_s)\frac{T_b - T_s}{\delta}, \tag{29}$$

where Se_l, Se_s, and δ are the Seebeck coefficients at the liquidus and solidus temperature, and the thickness of the molten pool. In these simulations, δ is about 50 μm. With the physical parameters in Tables V and VI, the estimated magnitude of the TECs is about 1.5×10^8 A/m^2 matching with the current simulation results.

To further analyze the effect of the Seebeck effect, the induced magnetic field, and Lorentz force density distribution in the middle cross section of the molten pool at $t = 120$ μs are given in Fig. 3. As convection in the induction

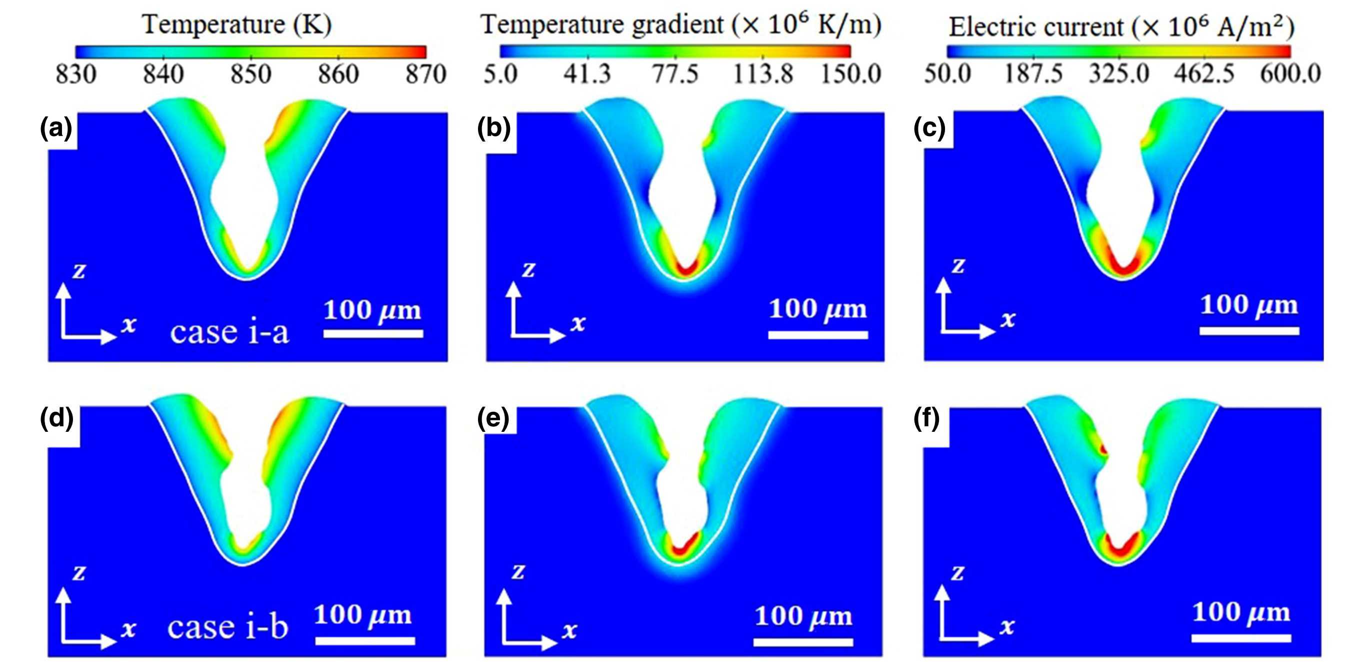

FIG. 2. Simulation results of stationary laser melting without external magnetic fields: (a),(d) temperature, (b),(e) temperature gradient, and (c),(f) electric currents in the middle cross section of the molten pool at $t = 120$ μs; (a)–(c) are the simulation results with the Seebeck effect (case i-a), whereas (d)–(f) are those without the Seebeck effect (case i-b). The white curves are the solid-liquid interfaces.

equation ($\mathbf{v} \times \mathbf{B}$) in Eq. (19) is small, the main component of the induced magnetic field is the Seebeck-effect-induced magnetic field ($\mathbf{b}_{\text{TECs}}$). The intensity of $\mathbf{b}_{\text{TECs}}$ is 1×10^{-5} T $- 1 \times 10^{-4}$ T as shown in Fig. 3(a). Here $\mathbf{b}_{\text{TECs}}$ is high on the solid-liquid interface, especially in the bottom of the molten pool, and decreases with the distance increase on both sides, which agrees with the laser welding simulation results by Chen *et al.* [19]. The induced magnetic field is the result by the outer product of ∇Se and ∇T where ∇Se is zero in the same phase and not continuous on the solid-liquid interface. Moreover, the higher temperature gradient in the bottom of the molten pool leads to a larger induced magnetic intensity. In Fig. 3(b), the magnitude of the Lorentz force density in the molten pool ranges between 1×10^3 N/m^3 and 1×10^4 N/m^3. The Lorentz force is also higher in the bottom of the molten pool and the solid-liquid interface similar to the TECs. However, the Lorentz force in the upper part of the molten pool is much smaller than that in the bottom because the induced magnetic intensity is nearly zero in this region as shown in Fig. 3(a). Compared with the magnitude of the buoyancy force density ($\rho g a_v (T - T_l) \sim 1 \times 10^3$ N/m^3), the Lorentz force is nonnegligible, although it is localized.

The keyhole depths growth and z-direction recoil forces variation with time are given in Fig. 4 to study the effect of the Lorentz force in the laser melting process. In Fig. 4, both the keyhole depths and the z-direction recoil forces with and without the Seebeck effect share a similar trend as time increases. Before 50 μs, the molten pools are shallow with the keyhole depths being lower than 100 μm. The

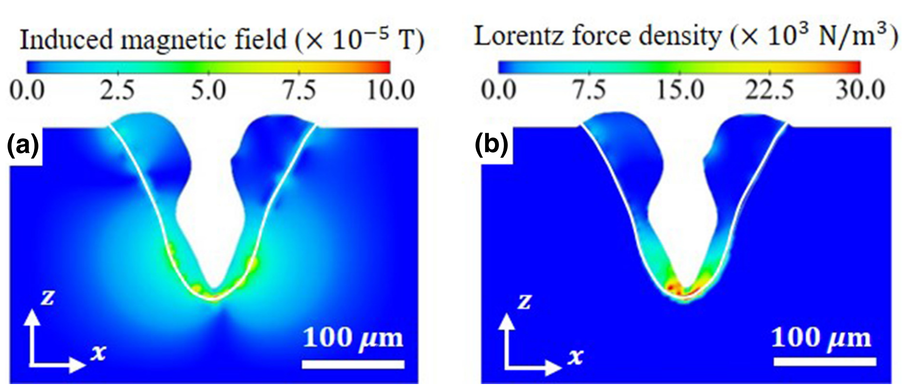

FIG. 3. Simulation results of case i-a: (a) induced magnetic field and (b) Lorentz force density in the middle cross section of the molten pool at $t = 120$ μs. The white curves are the solid-liquid interfaces.

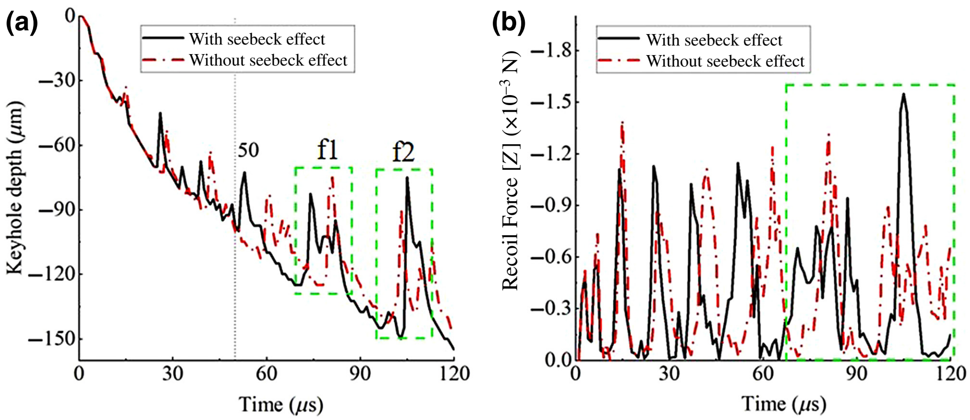

FIG. 4. Comparison of the (a) keyhole depths below the plate surface and (b) z-direction recoil forces on the keyhole surface. The black solid lines and red dashed lines are the simulation results with and without the Seebeck effect, respectively. f1 and f2 are the two main fluctuations. The black solid and red dashed lines are the results of cases i-a and i-b, respectively.

z-direction recoil forces in the two simulations range from 1×10^{-4} N to 1.5×10^{-3} N. However, the differences of the keyhole depth fluctuation and the z-direction recoil force between the two simulations after 70 μs are obvious. There are two main keyhole fluctuations in the two simulations as shown in the two green dashed rectangles of Fig. 4(a) (f1 and f2). The amplitudes of these fluctuations are given in Table III, and the difference of f1 and f2 between case i-a and case i-b are 17.6% and 30.0%. The fluctuation of the z-direction recoil forces in this period is also not consistent as shown in the green dashed rectangle of Fig. 4(b). The sequences of the z-direction recoil force fluctuation between the two simulations are reversed after 70 μs. These differences suggest that the Seebeck effect is stronger with the increase of the keyhole depth. Although the Lorentz force by the Seebeck effect on the molten pool dynamics is local, especially in the bottom part, the amplitude of it is comparable to the buoyancy force density and can also change the keyhole fluctuation and recoil force distribution in the laser melting process.

B. Stationary laser melting under different external magnetic fields

To analyze the influence of the external magnetic fields in the laser melting process, the static external magnetic fields along the y and z direction are assigned in the stationary laser melting simulations (cases ii and iii). The simulation results of the temperature, temperature gradient, electric current, and Lorentz force density of the molten pool in the middle cross section are presented in Fig. 5, where the series (a), (b), (c), and (d) represent the results of simulation cases ii-a, ii-b, iii-a, and iii-b, respectively. The keyhole depths of the series (a), (b), (c), and (d) are 125.0 μm, 127.5 μm, 130 μm, and 140 μm at $t = 110$ μs. The relative differences in cases ii and iii are 2.0% and 7.7%, respectively. In Fig. 5, the temperature, temperature gradient, and electric current distribution of the four simulations are similar to the results without an external magnetic field in Fig. 2 and the values of these variables are higher in the upper and bottom parts of the molten pool. The temperature gradients and electric currents in the four cases are about 1×10^8 K/m and 3×10^8 A/m^2. It is the reason that the TECs ($|\sigma Se \nabla T| \sim 10^8$ A/m^2) is much larger than the electric current by the convection ($|\sigma \mathbf{v} \times \mathbf{B}| \sim 10^6$ A/m^2). In other words, the electric currents in the molten pool are mainly composed of the TECs due to the high-temperature gradient.

TABLE III. Amplitudes of the keyhole depth fluctuations.

Fluctuation	Case i-a	Case i-b
f1	125.0 μm	130.0 μm
f2	127.5 μm	140.0 μm

The Lorentz force density distributions in Figs. 5(a4)–5(d4) are not like the result in Fig. 3(b) but similar to the distributions of the temperature gradient and electric current in Fig. 5. The Lorentz force densities are not only high in the bottom of the molten pool, but also strong in the whole molten pool. The magnitude of the Lorentz force densities in the inner region and surface of the molten pool is higher than that in the solid-liquid interface, similar to the distribution of electric current. Moreover, the magnitude of the Lorentz force density can reach 1.5×10^8 N/m^3, which is about four orders higher than the result without external magnetic fields.

To understand the Lorentz force density distributions, the intensity of induced magnetic fields in the middle cross sections of the molten pools are shown in Figs. 6(a) and 6(b). Although the intensities of induced magnetic fields are still $1 \times 10^{-5} - 1 \times 10^{-4}$ T, the distribution of the induced magnetic fields are different from the simulation results without external magnetic fields in Fig. 3(a). The induced magnetic fields are not only high on the solid-liquid interface but also remarkable in the inner part of the molten pool, where the amplitude of the fluid velocity is higher as shown in Figs. 6(c) and 6(d). The convection induced magnetic field ($\mathbf{b}_c$) can be

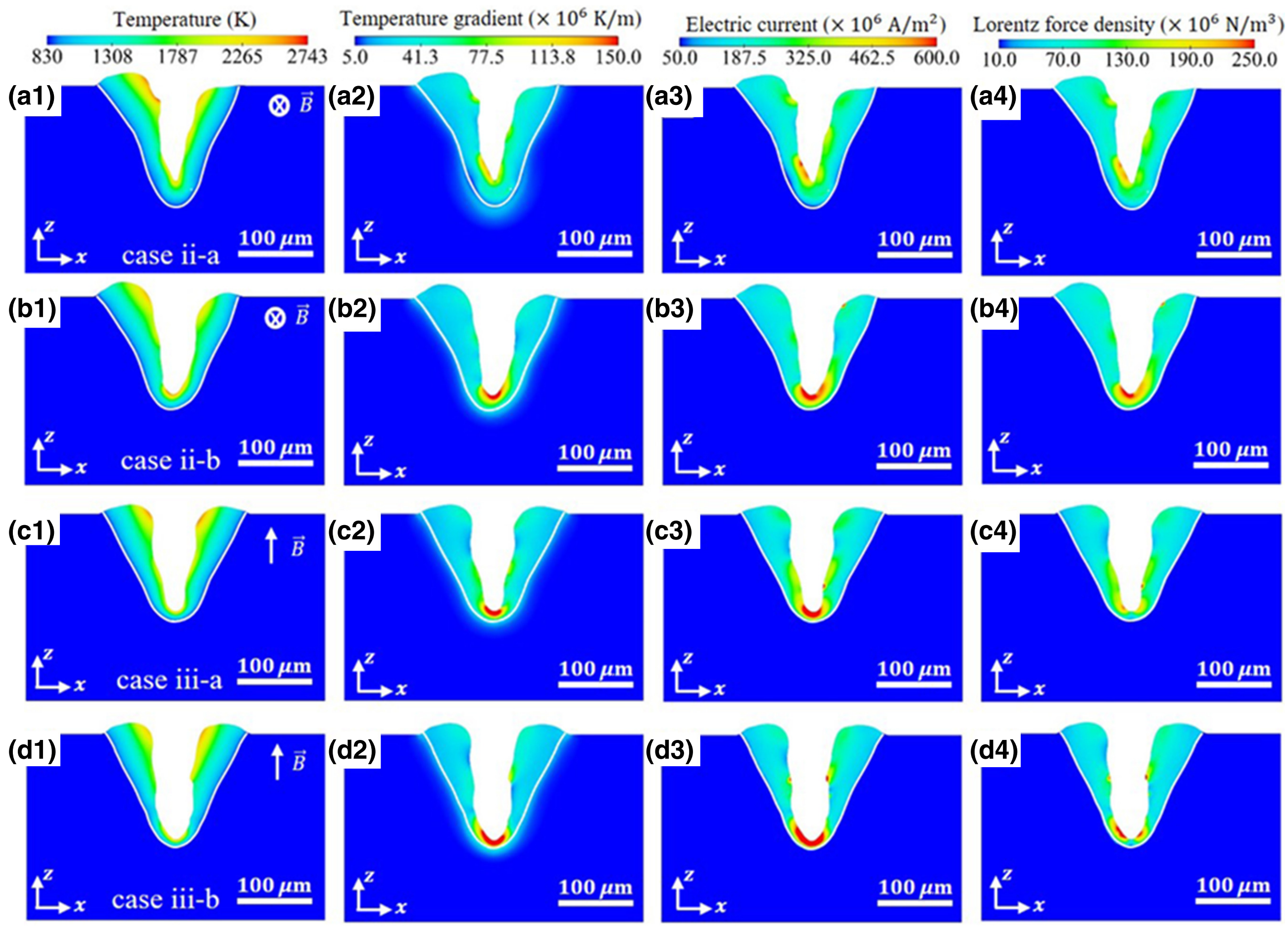

FIG. 5. Simulation results of stationary laser melting under different external magnetic fields in the middle cross section of the molten pool at $t = 110$ μs. Series (1), (2), (3), and (4) are the temperature fields, temperature gradients, electric currents, and Lorentz force densities of the simulations, respectively. Series (a), (b), (c), and (d) are the results for case ii-a, ii-b, iii-a, and iii-b, respectively.

estimated with Ampere's law [31] and the intensity of $\mathbf{b}_c$ is $\sim \mu_0 l\sigma_c|\mathbf{v}||\mathbf{B}_0| = \mathrm{Re}_m|\mathbf{B}_0|$, where l and $|\mathbf{v}|$ are the thickness and velocity of the fluid domain and Re_m is the magnetic Reynolds number. With the values of $l \approx 50$ μm, $v \approx 3$ m/s, $\sigma_c = 4.0 \times 10^6$ S/m, and $|\mathbf{B}_0| = 0.4$ T, we can estimate that $|\mathbf{b}_c|$ is about 1×10^{-4} T comparable to the Seebeck-effect-induced magnetic field ($\mathbf{b}_{\mathrm{TECs}}$). Therefore, the intensity of induced magnetic fields are determined by the Seebeck effect and the molten pool dynamics together. But the intensity of the induced magnetic fields ($\mathbf{b}$) is lower than 1% of the external magnetic field ($\mathbf{B}_0$) magnitude. In this situation, the whole magnetic field can be taken as the external magnetic field. With these evenly distributed magnetic fields, the distribution of the Lorentz force densities are similar to the distributions of the electric currents as shown in Fig. 5.

In Fig. 7, the keyhole depths below the plate surface and z-direction recoil forces under different external magnetic fields are given to reveal the influence of the induced magnetic fields on the keyhole fluctuation. The keyhole depth growing pattern and the z-direction recoil forces fluctuation with and without induced magnetic fields are consistent with each other, and all the keyhole depths reach 150 μm around 120 μs under different external magnetic fields in Fig. 7(a). The z-direction recoil forces all range between 1×10^{-4} N and 1.5×10^{-3} N under the y- and z-direction external magnetic field in Fig. 7(b). The main differences of the keyhole depth and z-direction recoil force curves are the time-phased difference at $t > 50$ μs, which is the reason of the Lorentz force by the TECs and induced magnetic field. But the time difference is lower than 10 μs and is acceptable for the simulation validity.

Comparing the keyhole depth curves in Figs. 4(a), 7(a), and 7(b), these six curves share similar growth trend. However, the keyhole depth curves in Figs. 7(a) and 7(b) are smooth and have six main fluctuations, whereas the keyhole growth curves in Fig. 4(a) are rough and even blur some main fluctuations. It indicates that the Lorentz force under the external magnetic fields can reduce the local

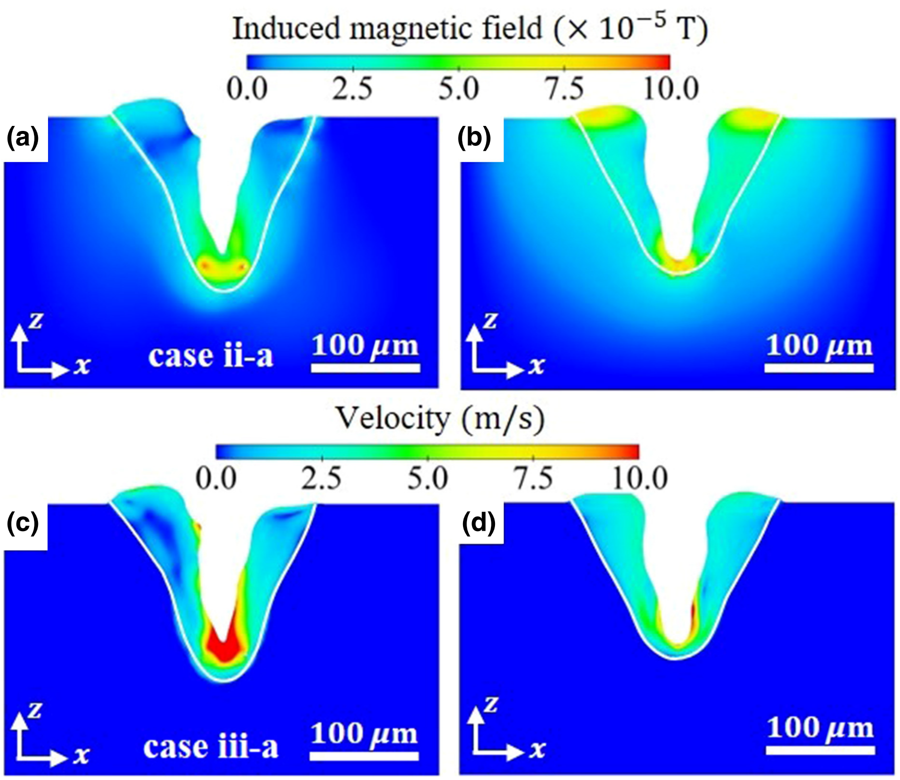

FIG. 6. (a),(b) Intensity of the induced magnetic fields and (c),(d) Velocity in the middle cross section of the molten pool at $t = 110$ μs under different external magnetic fields: (a) and (c) are the results of simulation case ii-a, whereas (b) and (d) are the results of simulation case iii-a. The white curves are the solid-liquid interfaces.

fluctuations in the bottom of the molten pool. Furthermore, the z-direction recoil forces in Figs. 7(c) and 7(d) vary between 1×10^{-4} N and 1.5×10^{-3} N, and these curves are much more regular than the curves in Fig. 4(b), especially at $t > 70$ μs. These keyhole depths and z-direction recoil forces variations suggest that the induced magnetic field can be ignored with a larger external magnetic field, whereas it should be considered without

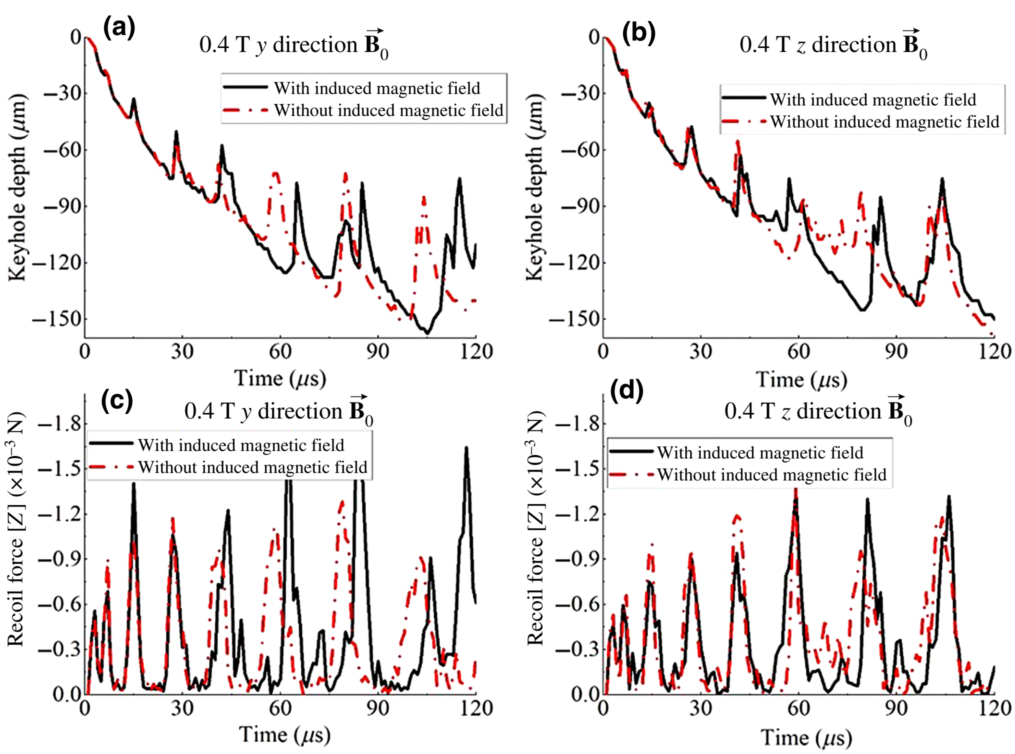

FIG. 7. (a),(b) Keyhole depths below the plate surface and (c),(d) z-direction recoil forces with different external magnetic fields: (a),(c) are the results of simulation cases ii-a and ii-b, whereas (b),(d) are the results of simulation cases iii-a and iii-b.

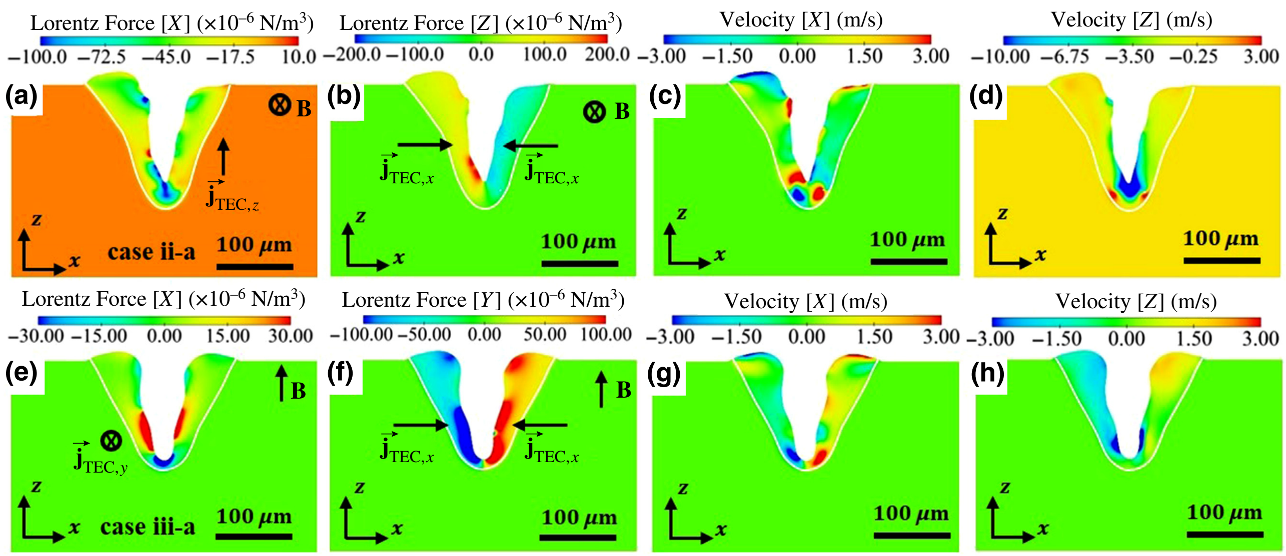

FIG. 8. (a),(b),(e),(f) Lorentz force density components and (c),(d),(g),(h) velocity components in the middle cross sections: (a)–(d) and (e)–(h) are the results of simulation cases ii-a and iii-a, respectively. The white curves are the solid-liquid interfaces.

external magnetic fields to obtain accurate molten pool dynamics in the laser melting simulation.

It should be pointed out that the middle cross sections of the molten pool are not symmetric in Figs. 5(a) and 5(b) series (ii-a and ii-b), whereas the other two simulation results (iii-a and iii-b) in Fig. 5 are symmetric. Taking Figs. 5(a) and 5(c) series as examples, the height above the bare plate on the left side of the molten pool is 17.5 μm, whereas that on the right side molten pool is lower than 1.0 μm in case ii-a. In Fig. 5(c) series the heights above the bare plate on the left and right sides of the molten pool are 11.3 μm and 8.8 μm, respectively. The difference of the molten pool shape is caused by the results of the Lorentz force distributions, which are presented in Fig. 8.

As the TECs and external magnetic field are the main components of the electric current and magnetic field, the direction of the Lorentz force is determined by the temperature gradient and the external magnetic field. Thus, the Lorentz forces are not opposed to the direction of molten pool velocity to damp the fluid flow as shown in Fig. 8, and the Lorentz force density components are different under the different external magnetic fields. In case ii-a, the x component of the Lorentz force density is negative in the middle cross section of the molten pool as shown in Fig. 8(a), which is not opposed to the velocity direction in Fig. 8(c), and this negative Lorentz force drives the molten pool to the left. The asymmetric distribution molten pool further influences the temperature distribution and leads to an asymmetric z component of the Lorentz force distribution as shown in Fig. 8(b). In case iii-a, the y component of the Lorentz force density in the middle cross section is symmetric as shown in Fig. 8(f). The x component of the Lorentz force is small as shown in Fig. 8(e), because the temperature gradient along the y direction in the middle cross section is small. Thus, under the z-direction external magnetic field, the Lorentz force density components and molten pool shape are symmetric.

The Lorentz force components under the y and z direction external magnetic fields are presented in Fig. 9. It is obvious that the Lorentz force components variations are similar with and without induced magnetic fields. It verifies that the induced magnetic field can be ignored with such external magnetic fields. Moreover, the variations of the Lorentz force components with different magnetic fields are different. In Figs. 9(a) and 9(b), the magnitudes of the Lorentz force components in the molten pool under the y-direction external magnetic field are increasing with the laser heating time, whereas the magnitude of the Lorentz force components under the z-direction external magnetic field in Figs. 9(c) and 9(d) are fluctuating around zero. Under the y-direction external magnetic field, the magnitude of the x-direction Lorentz force reaches 5×10^{-5} N, about 20 times higher than the magnitude of the Lorentz force components under the z-direction external magnetic field. This further explains that the shape of the molten pool is asymmetric under the y-direction external magnetic field and symmetric under the z-direction external magnetic field.

C. Laser scanning under different external magnetic fields

To analyze the influence of Lorentz force in the SLM process, single-track laser scanning on a bare plate under the different external magnetic fields is simulated at a

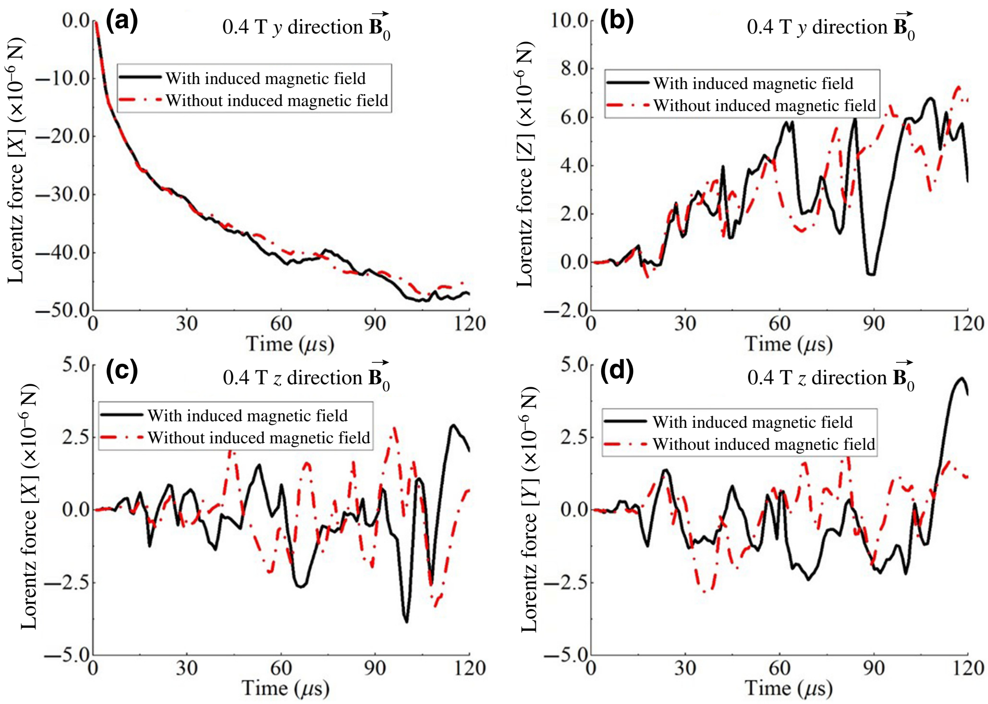

FIG. 9. Lorentz force components: (a),(b) under the y-direction external magnetic field; (c),(d) under the z-direction external magnetic field.

laser scanning speed of 1.0 m/s along the x direction, and the magnetic components are listed in Table II. Based on the analysis of stationary laser melting simulations, the induced magnetic field is considered for case 1, whereas the other two cases are conducted without induced magnetic field.

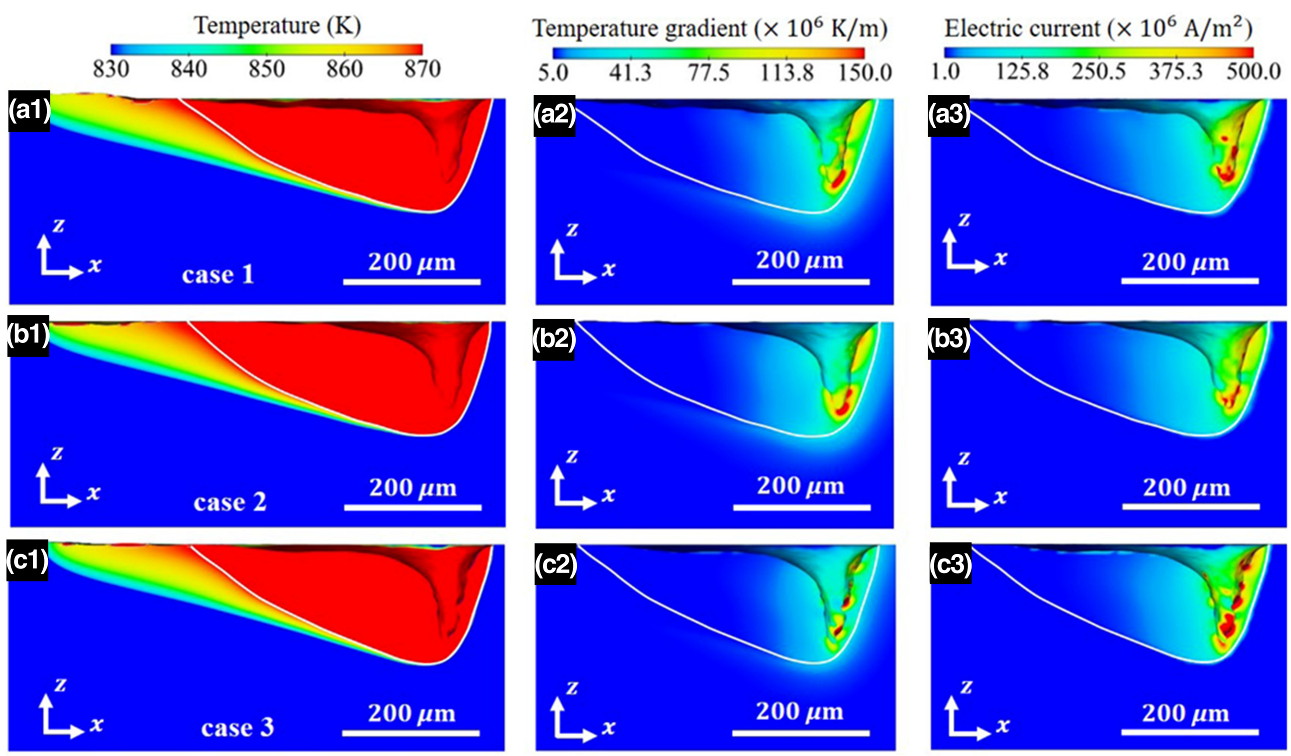

FIG. 10. Simulation results of laser scanning: (a1),(b1),(c1) temperature, (a2),(b2),(c2) temperature, gradient and (a3),(b3),(c3) electric current in the molten pool at $t = 108$ μs. The series (a), (b), and (c) are the results of cases 1, 2, and 3, respectively. The white curves are the solid-liquid interfaces.

TABLE IV. Geometry features of the molten pool.

	Case 1	Case 2	Case 3
Length of the molten pool (μm)	680	668	656
Width of the molten pool (μm)	238	226	222
Length of the liquidus region (μm)	444	452	432
Average keyhole depth (μm)	129.0	129.6	147.8
Variance of the keyhole depth (μm^2)	221.4	207.0	311.5

In Fig. 10, the molten pools are nearly stable at $t = 108$ μs with similar shapes. The magnitude and distribution of the temperature gradient and electric current of the three simulation results are similar in Fig. 10. The temperature gradient and electric current density in front of the keyhole reach 1.5×10^8 K/m and 5.0×10^8 A/m^2, which are much higher than those behind the keyhole. The temperature gradient and electric current behind the keyhole rapidly drop below 1.0×10^6 K/m and 1.0×10^6 A/m^2 as the distance to the keyhole increases. Moreover, the length and width of the molten pool and length of the liquidus region (the region with $T \geq T_l$) are given in Table IV. The difference of the molten pool length and width and liquidus region length due to the external magnetic fields are smaller than 3.5%, 6.7%, and 2.7%, respectively. The energy absorptions of the three cases fluctuate between 45% and 47%, matching with Trapp's experiment [29]. This indicates that the overall shape of the molten pool is mainly determined by the absorbed energy and the effect of the external magnetic field is not obvious.

However, the average keyhole depths below the plate surface and variances of the keyhole depth in the three simulations are different as listed in Table IV. The keyhole depth and its variance in case 3 is about 14.0% deeper and 40.0–50.0% higher than those in the other two simulation cases. In Fig. 11, the keyhole depth below the plate surface and z-direction recoil force in case 3 are different from those of cases 1 and 2. The keyhole depths in cases 1 and 2 fluctuate between 90 and 150 μm, whereas it ranges from 90 to 180 μm in case 3 as shown in Fig. 11(a). In Fig. 11(b), the z-direction recoil forces in case 1 and 2 are lower than 1.0×10^{-3} N, whereas it can reach 1.5×10^{-3} N in case 3. This indicates that the z-direction external magnetic field has a stronger effect on the molten pool bottom vibration in the SLM process compared with the other two simulation cases.

To further analyze the influence of the external magnetic field on the molten pool dynamics, the magnitudes of the molten pool velocity, streamlines of the molten pool, and Lorentz force densities are presented in Fig. 12. The magnitudes and distributions of the molten pool velocity in the three simulations are similar as shown in Figs. 12(a1)–12(a3). The velocity magnitude around the keyhole is higher than other regions of the molten pool: the fluid velocity on the upper and bottom regions of the keyhole is greater than 4 m/s, whereas the fluid velocity near the solid-liquid interface is lower than 1 m/s.

Interestingly, the streamlines in the molten pool in these three simulations are different from each other. In case 1, there are two regions in the molten pool behind the keyhole in Fig. 12(b1) and Movie 1 within the Supplemental Material [36]: the circulation region (Region 1) and spiral rotating region (Region 2). The circulation region is behind the keyhole with a vortex rotating nearly vertical to the y direction. This region has been directly observed using the *in situ* x-ray imaging by Hojjatzadeh *et al.* [30], which could trap bubbles in the molten pool and result in pores in the as-built parts. Behind the circulation region, there is a spiral rotating region where the liquid metal rotates spirally from the inner front part of the molten pool to the outside rear part of the molten pool. This region in the simulation matches with the *in situ* x-ray imaging by Guo *et al.* [37]. In case 2, the vortex intensity in the circulation region decreases, and the streamline is relatively smooth as shown in Fig. 12(b2) and Movie 2 within the Supplemental Material [36]. The spiral rotating region shrinks from the mush zone to the liquid region. In Fig. 12(b3) and Movie 3 within the Supplemental Material [36], the circulation region nearly disappears and the size of the spiral rotating region is further decreases in case 3. It indicates that the

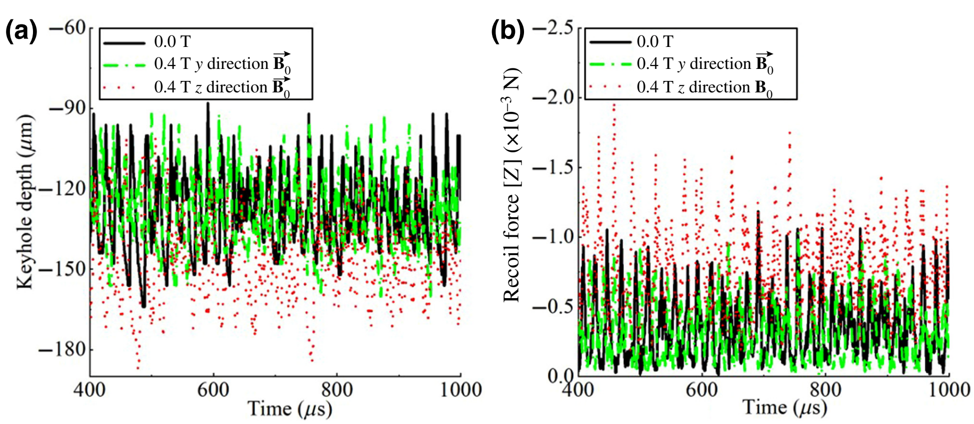

FIG. 11. Comparison of (a) keyhole depths below the plate surface and (b) z-direction recoil forces in the three simulation cases.

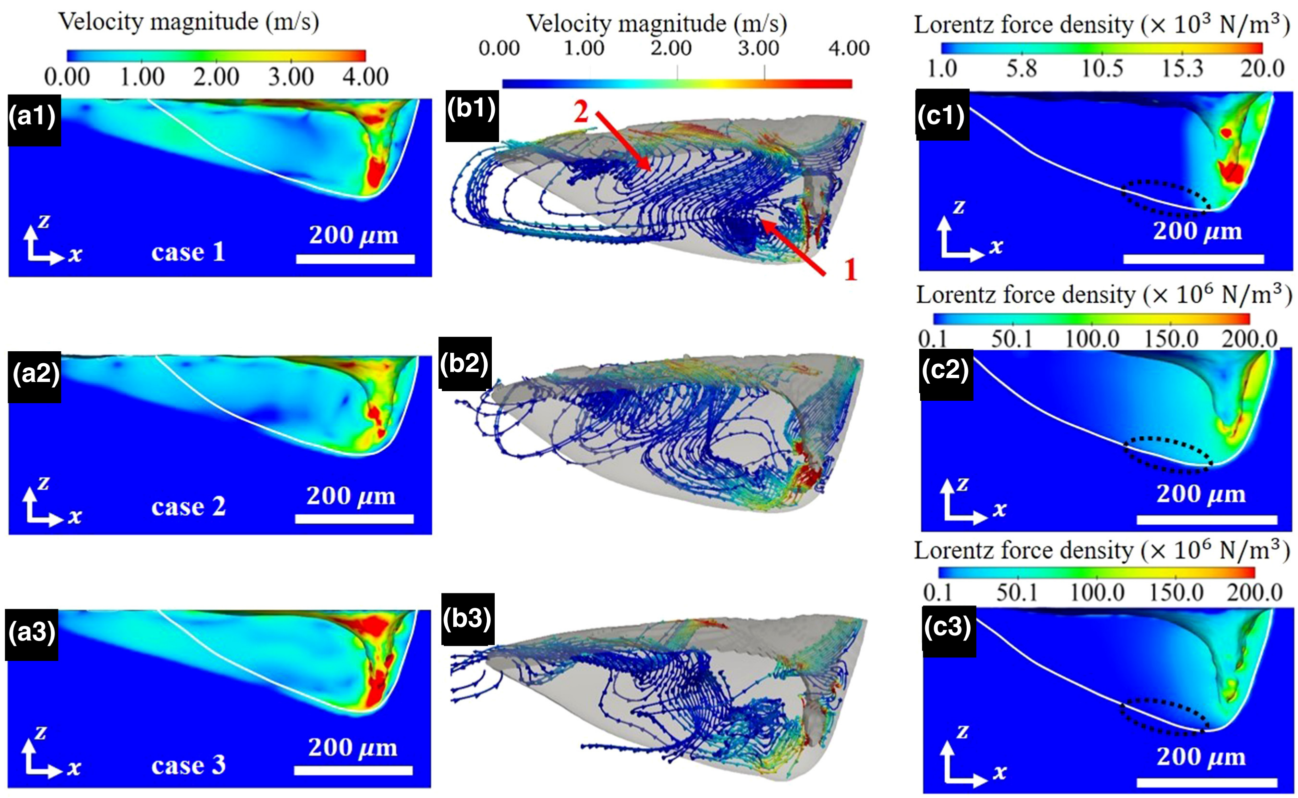

FIG. 12. Simulation results of laser scanning: (a) velocity magnitudes, (b) streamlines, and (c) Lorentz force density distribution in the molten pool. Series (1), (2), and (3) are the results of cases 1, 2, and 3, respectively. The white curves in series (a) and the gray surfaces in series (b) are the solid-liquid interfaces. Region 1 and Region 2 in (b1) are the circulation region and spiral rotating region, respectively. The black dashed regions in series (c) are the effective solidification front.

external magnetic field can be a useful tool to control the liquid flow in the molten pool.

In Fig. 12(c), the distributions of the Lorentz force density in the three simulations are similar, which are high around the keyhole region. However, the magnitudes of the Lorentz force density are lower than 2×10^4 N/m^3 in case 1, which is about four orders lower than those of case 2 and 3. It is the reason that magnetic intensity without an external magnetic field is much lower than those under the external magnetic fields in the SLM process as mentioned in the stationary laser melting simulations.

Furthermore, the Lorentz force has been proven to be able to influence the dendritic morphology in the metal solidification process. In previous experiments [7,11,12], the dendritic morphology transited from columnar to equiaxed with the increase of magnetic intensity during the metal solidification process. In the SLM process, the depth of the molten pool is larger than the thickness of the powder bed (about 40–100 μm), the upper part of the current laser scanning track would be remelted in the laser scanning of next layer and the effective solidification front region is the solid-liquid interface in the bottom part of the molten pool as shown in the black dashed region in Fig. 12(c). Under the external magnetic fields, the Lorentz force density can reach 1×10^5–1×10^6 N/m^3 in the effective solidification front, whereas the Lorentz force density is lower than 5×10^3 N/m^3 in case 1. The experiments by Li *et al.* [12] show that the Lorentz force density larger than 1×10^5 N/m^3 can change the dendritic morphology from columnar to equiaxed. The SLM experimental parameters used by Du *et al.* [7] are similar to the current simulation, and they also observed that the percentage of equiaxed grains increases under the z-direction external magnetic field. These experimental results validate the current model indirectly. To improve the effectiveness and applicability of the current TEMHD in metal additive manufacturing, we are planning to conduct more experiments on grain size transition with external magnetic field in the future.

Although the magnitude of the Lorentz force densities are similar, the Lorentz force density components are different as shown in Fig. 13. In case 2, the Lorentz force is along the negative z negative x direction in front of the keyhole and positive z negative x direction behind the keyhole as shown in Figs. 13(a1) and 13(a2), which drives the liquid metal towards the bottom and then to the surface along with the negative x direction in the molten pool. However, the Lorentz force density components in Figs. 13(b1) and 13(b2) are rotating around the keyhole

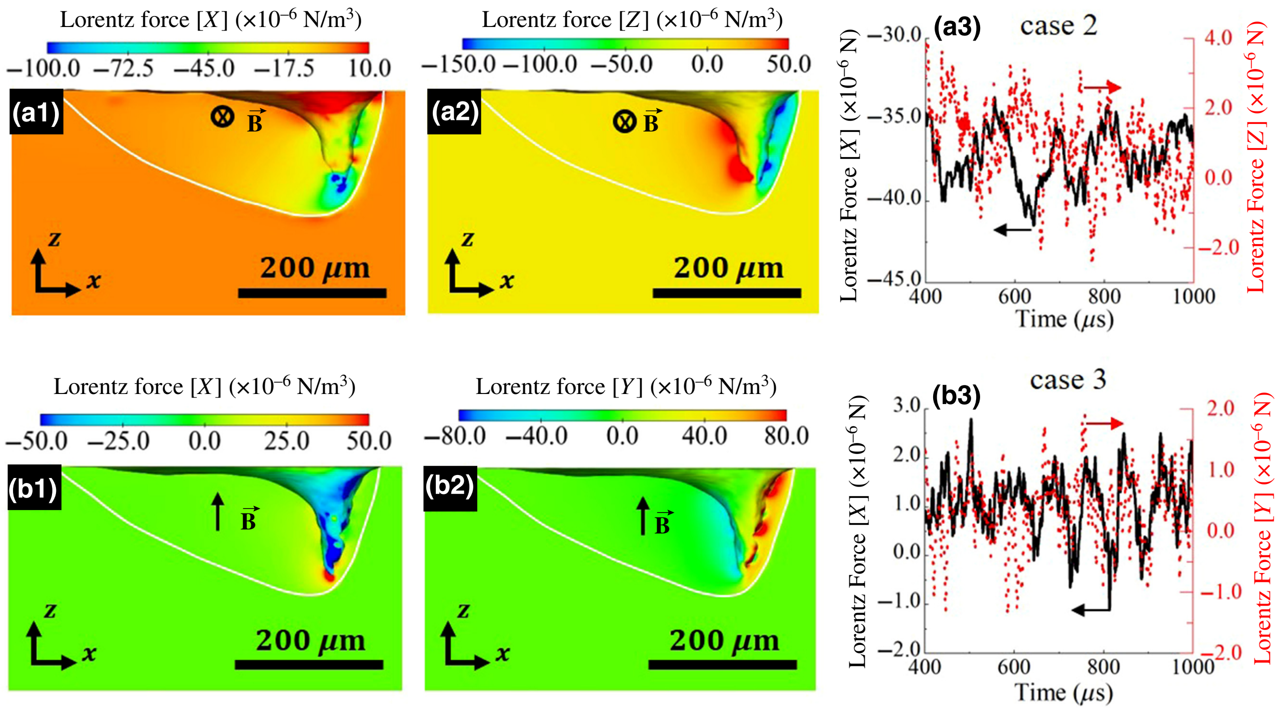

FIG. 13. Components of the Lorentz force density distribution (a1),(a2),(b1),(b2) and Lorentz forces (a3),(b3) of cases 2 and 3 at $t = 108$ μs. Series (a) and (b) are the results of cases 2 and 3, respectively. The white curves are the solid-liquid interfaces.

anticlockwise (from the top view), which stirs the liquid flow. These Lorentz force density distribution patterns suggest that the y- and z-direction magnetic fields can both generate Lorentz forces that are sufficient to influence the molten pool flow, but the directions of the Lorentz forces are different.

In Fig. 13(a3) the z component of the Lorentz force in case 2 fluctuates around zero, and the magnitude is lower than 4×10^{-6} N. However, the x-component Lorentz force is about -3×10^{-5} N, which is comparable to the z-direction recoil force at valley point (about -1×10^{-4} N) as shown in Fig. 11(b). This indicates that the Lorentz force in case 2 drives the fluid to the negative x direction. In case 3, both the x and y components of the Lorentz force vibrate around zero with an amplitude lower than 3×10^{-6} N in Fig. 13(b3). This means that the magnitude of the Lorentz force in case 3 is symmetrically distributed in the molten pool around the keyhole under the z-direction external magnetic field, although it can rotate the liquid metal in the molten pool as shown in Figs. 13(b1) and 13(b2).

IV. CONCLUSIONS

In this study, an electrodynamic model with the Seebeck effect has been implemented in the multiphysics thermal-fluid flow model to build a TEMHD model. The numerical simulation results show that the electric current in the SLM process is mainly composed of the TECs, and the induced magnetic field can be ignored compared with the high external magnetic intensity.

In the stationary laser melting simulations, the Lorentz force is relatively high in the bottom of the molten pool, and the magnitude is comparable to the buoyancy force density, which can influence the molten pool dynamics especially in deep keyhole mode without external magnetic fields. Under the external magnetic fields, the molten pool dynamics with and without incorporating the induced magnetic field are similar. The Lorentz force densities under the external magnetic fields reach 1.5×10^8 N/m^3 and are about four orders of magnitude higher than that without an external magnetic. Such Lorentz force density is sufficient to make a difference in the molten pool shape.

In the laser scanning simulations, although the Lorentz forces under the y- and z-direction external magnetic fields distribute differently, both of them can suppress the fluid circulation and decrease the fluid spiral rotating behind the keyhole in the molten pool. Moreover, the Lorentz force in the bottom of the molten pool is strong enough to transit the columnar grains to equiaxed grains under external magnetic fields. Thus, an external magnetic field can be a useful tool to control the molten pool flow and grain growth in the SLM process.

ACKNOWLEDGMENTS

This research is supported by A*STAR under its AME IRG Grant (Project No. A20E5c0091).

APPENDIX A: MATERIAL PROPERTIES

TABLE V. Thermophysical properties of AlSi10Mg [7,30,38].

Property	Value
Solidus temperature (T_s, K)	830
Liquidus temperature (T_l, K)	870
Boiling temperature (T_b, K)	2743
Density (ρ, kg/m^3)	2680
Latent heat of melting (L_m, J/kg)	3.89×10^5
Latent heat of evaporation (L_v, J/kg)	1.07×10^7
Saturated vapor pressure (P_e, Pa)	1.013×10^5 (T_b=2743 K)
Surface tension coefficient (σ_0, N/m)	1.02
Temperature sensitivity of surface tension (σ_s^T, N/(m · K))	3.1×10^{-4}
Linear thermal expansion coefficient (α_v, 1/K)	2.3×10^{-5}
Convective heat transfer coefficient (h_c, W/(m · K))	82
Radiation emissivity, ϵ	0.4
Electrical conductivity of liquid (σ_c, S/m)	4.0×10^6
Liquidus Seebeck coefficient (Se_l, V/K)	-2.5×10^{-6}
Solidus Seebeck coefficient (Se_s, V/K)	-1.5×10^{-6}

TABLE VI. Temperature-dependent thermophysical properties of AlSi10Mg [30].

Property	Temperature (T, K)	Value
Dynamic viscosity (μ, Pa · s)	875	0.0022
	1000	0.00125
	1450	0.0007
	1850	0.00058
	2250	0.00045
	2700	0.0004
Thermal conductivity (k, W /(m · K))	300	160
	400	160
	500	160
	600	160
	700	160
	830	110
	870	90
	1200	100
	1500	110
	1800	115
	2100	120
Specific heat (C_p, J /(kg · K))	300	900
	375	960
	575	1020
	775	1125
	940	1040
	960	1040
	1100	1075
	1562	1075

APPENDIX B: NUMERICAL CONVERGENCE

In the current simulation, the pressure, heat transfer, induction, and electric potential equations are solved with an implicit numerical scheme. The convergence of the linear system is

$$\|r\|_1 = \epsilon, \tag{B1}$$

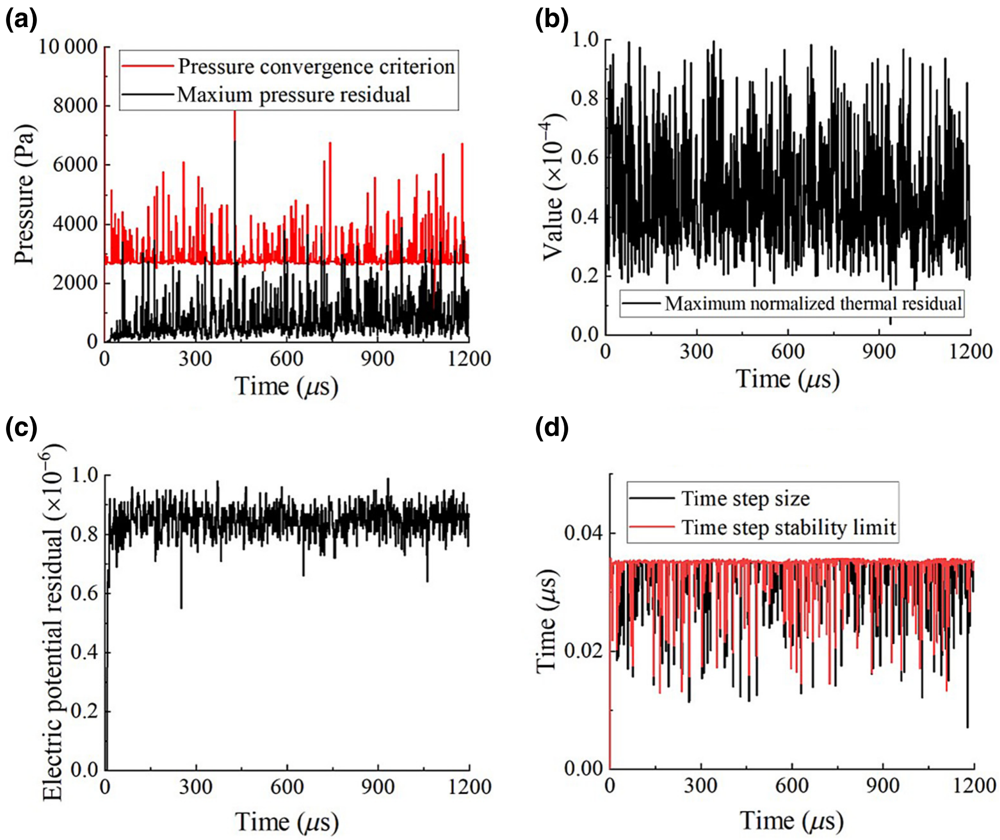

FIG. 14. Numerical convergence of case 3: (a) pressure convergence; (b) thermal convergence; (c) electric potential convergence; and (d) time step limit.

where $\|r\|_1$ is the first norm of the residual of the linear system and ϵ is the convergence criterion that is used to determine at what point the values have converged. Taking case 3 as an example, the numerical convergence results are given in Fig. 14, where the pressure, energy, and electric potential equations are converged. The value for pressure convergence is automatically computed by FLOW-3D and is fluctuating around 3×10^3 Pa in the current simulations, as shown in Fig. 14(a). The normalized thermal convergence criterion is 1×10^{-4}. For induced equation and electric potential equation, the value of ϵ is 1×10^{-6} V. To ensure the stability of numerical calculation, the time step is limited below $\sim 0.38\ \mu$s.

[1] P. de Rango, M. Lees, P. Lejay, A. Sulpice, R. Tournier, M. Ingold, P. Germi, and M. Pernet, Texturing of magnetic materials at high temperature by solidification in a magnetic field, Nature **349**, 770 (1991).

[2] D. Du, Y. Fautrelle, Z. Ren, R. Moreau, and X. Li, Effect of a high magnetic field on the growth of ternary Al-Cu-Ag alloys during directional solidification, Acta Mater. **121**, 240 (2016).

[3] N. Kang, P. Coddet, J. Wang, H. Yuan, Z. Ren, H. Liao, and C. Coddet, A novel approach to in-situ produce functionally graded silicon matrix composite materials by selective laser melting, Compos. Struct. **172**, 251 (2017).

[4] Z. Yan, X. Li, Z. Cao, X. Zhang, and T. Li, Grain refinement of horizontal continuous casting of the CuNi10Fe1Mn alloy hollow billets by rotating magnetic field (RMF), Mater. Lett. **62**, 4389 (2008).

[5] Z. Yan, M. Chen, Y. Teng, J. Yang, L. Yang, and H. Gao, Forced flow and solidification process of Sn-3.5%Pb melt in hollow billet under rotating magnetic field, J. Mater. Eng. Perform. **24**, 1059 (2015).

[6] K. Timmel, S. Eckert, and G. Gerbeth, Experimental investigation of the flow in a continuous-casting mold under the influence of a transverse, direct current magnetic field, Metall. Mater. Trans. B **42**, 68 (2011).

[7] D. Du, J. C. Haley, A. Dong, Y. Fautrelle, D. Shu, G. Zhu, X. Li, B. Sun, and E. J. Lavernia, Influence of static magnetic field on microstructure and mechanical behavior of selective laser melted AlSi10Mg alloy, Mater. Des. **181**, 107923 (2019).

[8] A. Kao, T. Gan, C. Tonry, I. Krastins, and K. Pericleous, Thermoelectric magnetohydrodynamic control of melt pool dynamics and microstructure evolution in additive manufacturing, Philos. Trans. R. Soc., A **378**, 20190249 (2020).

[9] S. Vader, Z. Vader, I. H. Karampelas, and E. P. Furlani, Advances in magnetohydrodynamic liquid metal jet printing, TechConnect Briefs **4**, 41 (2016).

[10] V. Sukhotskiy, I. Karampelas, G. Garg, A. Verma, M. Tong, S. Vader, Z. Vader, and E. Furlani, Magnetohydrodynamic drop-on-demand liquid metal 3D printing, Proc. Solid Freeform Fabr. (2017).

[11] X. Li, Y. Fautrelle, A. Gagnoud, D. Du, J. Wang, Z. Ren, H. Nguyen-Thi, and N. Mangelinck-Noel, Effect of a weak

transverse magnetic field on solidification structure during directional solidification, Acta Mater. **64**, 367 (2014).

[12] X. Li, A. Gagnoud, Y. Fautrelle, Z. Ren, R. Moreau, Y. Zhang, and C. Esling, Dendrite fragmentation and columnar-to-equiaxed transition during directional solidification at lower growth speed under a strong magnetic field, Acta Mater. **60**, 3321 (2012).

[13] Y. Fautrelle, J. Wang, G. Salloum-Abou-Jaoude, L. Abou-Khalil, G. Reinhart, X. Li, Z. M. Ren, and H. Nguyen-Thi, Thermo-electric-magnetic hydrodynamics in solidification: In situ observations and theory, JOM **70**, 764 (2018).

[14] B. Cai, A. Kao, E. Boller, O. Magdysyuk, R. Atwood, N. Vo, K. Pericleous, and P. Lee, Revealing the mechanisms by which magneto-hydrodynamics disrupts solidification microstructures, Acta Mater. **196**, 200 (2020).

[15] J. A. Shercliff, Thermoelectric magnetohydrodynamics, J. Fluid Mech. **91**, 231 (1979).

[16] X. Li, Y. Fautrelle, Z. Ren, and R. Moreau, Formation mechanism of axial macrosegregation of primary phases induced by a static magnetic field during directional solidification, Sci. Rep. **7**, 45834 (2017).

[17] S. N. Tewari, R. Shah, and H. Song, Effect of magnetic field on the microstructure and macrosegregation in directionally solidified Pb-Sn alloys, Metall. Mater. Trans. A **25**, 1535 (1994).

[18] J. Wang, Z. Ren, Y. Fautrelle, X. Li, H. Nguyen-Thi, N. Mangelinck-Noel, G. S. A. Jaoude, Y. Zhong, I. Kaldre, and A. Bojarevics, Modification of liquid/solid interface shape in directionally solidifying Al–Cu alloys by a transverse magnetic field, J. Mater. Sci. **48**, 213 (2013).

[19] X. Chen, S. Pang, X. Shao, C. Wang, J. Xiao, and P. Jiang, Three-dimensional transient thermoelectric currents in deep penetration laser welding of austenite stainless steel, Opt. Lasers Eng. **91**, 196 (2017).

[20] L. Cao, D. Liu, P. Jiang, X. Shao, Q. Zhou, and Y. Wang, Multi-physics simulation of dendritic growth in magnetic field assisted solidification, Int. J. Heat Mass Transfer **144**, 118673 (2019).

[21] W. Yan, W. Ge, J. Smith, S. Lin, O. L. Kafka, F. Lin, and W. K. Liu, Multi-scale modeling of electron beam melting of functionally graded materials, Acta Mater. **115**, 403 (2016).

[22] C. W. Hirt and B. D. Nichols, Volume of fluid (VOF) method for the dynamics of free boundaries, J. Comput. Phys. **39**, 201 (1981).

[23] L. Wang, Y. Zhang, and W. Yan, Evaporation Model for Keyhole Dynamics During Additive Manufacturing of Metal, Phys. Rev. Appl. **14**, 064039 (2020).

[24] J. Ahn and S.-J. Na, Three-dimensional thermal simulation of nanosecond laser ablation for semitransparent material, Appl. Surf. Sci. **283**, 115 (2013).

[25] T. Iida, Physical properties of liquid metals [I], J. Japan Welding Soc. **62**, 508 (1993).

[26] J. Xie, A. Kar, J. A. Rothenflue, and W. P. Latham, Temperature-dependent absorptivity and cutting capability of CO2, Nd:YAG and chemical oxygen–iodine lasers, J. Laser Appl. **9**, 77 (1997), publisher: Laser Institute of America.

[27] W. Pei, W. Zhengying, C. Zhen, L. Junfeng, Z. Shuzhe, and D. Jun, Numerical simulation and parametric analysis of selective laser melting process of AlSi10Mg powder, Appl. Phys. A **123**, 540 (2017).

[28] N. Kouraytem, X. Li, R. Cunningham, C. Zhao, N. Parab, T. Sun, A. D. Rollett, A. D. Spear, and W. Tan, Effect of Laser-Matter Interaction on Molten Pool Flow and Keyhole Dynamics, Phys. Rev. Appl. **11**, 064054 (2019).

[29] J. Trapp, A. M. Rubenchik, G. Guss, and M. J. Matthews, In situ absorptivity measurements of metallic powders during laser powder-bed fusion additive manufacturing, Appl. Mater. Today **9**, 341 (2017).

[30] S. M. H. Hojjatzadeh, N. D. Parab, W. Yan, Q. Guo, L. Xiong, C. Zhao, M. Qu, L. I. Escano, X. Xiao, K. Fezzaa, W. Everhart, T. Sun, and L. Chen, Pore elimination mechanisms during 3D printing of metals, Nat. Commun. **10**, 3088 (2019).

[31] P. A. Davidson, *Introduction to Magnetohydrodynamics*, Cambridge Texts in Applied Mathematics (Cambridge University Press, Cambridge, 2016), 2nd ed.

[32] D. Gu, Q. Shi, K. Lin, and L. Xi, Microstructure and performance evolution and underlying thermal mechanisms of Ni-based parts fabricated by selective laser melting, Addit. Manuf. **22**, 265 (2018).

[33] P. Yuan and D. Gu, Molten pool behaviour and its physical mechanism during selective laser melting of TiC/AlSi10Mg nanocomposites: Simulation and experiments, J. Phys. D: Appl. Phys. **48**, 035303 (2015).

[34] Y. Yang, X. Liu, and S. Wang, Thermal characteristics of induction heating with stepped diameter mold during two-phase zone continuous casting high-strength aluminum alloys, Int. J. Heat Mass Transfer **152**, 119479 (2020).

[35] P. S. Wei and F. K. Chung, Three-dimensional electron-beam deflection and missed joint in welding dissimilar metals, J. Heat Transfer **119**, 832 (1997).

[36] See Supplementary Material at http://link.aps.org/supplemental/10.1103/PhysRevApplied.15.064051 for streamline movies of case 1, case 2, and case 3.

[37] Q. Guo, C. Zhao, M. Qu, L. Xiong, S. M. H. Hojjatzadeh, L. I. Escano, N. D. Parab, K. Fezzaa, T. Sun, and L. Chen, In-situ full-field mapping of melt flow dynamics in laser metal additive manufacturing, Addit. Manuf. **31**, 100939 (2020).

[38] A. Lange, A. Cramer, and E. Beyer, Thermoelectric currents in laser induced melts pools, J. Laser Appl. **21**, 82 (2009).